Epitaxial growth of visible to infra-red transparent conducting In_2O_3 nanodot dispersions and reversible charge storage as a Li-ion battery anode

M. Osiak[1], W. Khunsin[2], E. Armstrong[1], T. Kennedy[3,4], C. M. Sotomayor Torres[2,5,6], K. M. Ryan[3,4], and C. O'Dwyer[1,4,7]

[1] *Department of Chemistry, University College Cork, Cork, Ireland*

[2] *Catalan Institute of Nanotechnology, Campus UAB, Edifici CM3, Bellaterra, 08193 (Barcelona) Spain*

[3] *Department of Chemical and Environmental Sciences, University of Limerick, Limerick, Ireland*

[4] *Materials and Surface Science Institute, University of Limerick, Limerick, Ireland*

[5] *Catalan Institute for Research and Advances Studies (ICREA), 08010 Barcelona, Spain*

[6] *Department of Physics, Universidad Autonoma de Barcelona, Campus UAB, 08193 Bellaterra, Spain*

[7] *Micro & Nanoelectronics Centre, Tyndall National Institute, Lee Maltings, Cork, Ireland*

Correspondence to: c.odwyer@ucc.ie; Tel: +353 21 4902732; Fax: +353 21 4274097

Abstract

Unique bimodal distributions of single crystal epitaxially grown In_2O_3 nanodots on silicon are shown to have excellent IR transparency greater than 87% at IR wavelengths up to 4 μm without sacrificing transparency in the visible region. These broadband antireflective nanodot dispersions are grown using a two-step metal deposition and oxidation by molecular beam epitaxy, and backscattered diffraction confirms a dominant (111) surface orientation. We detail the growth of a bimodal size distribution that facilitates good surface coverage (80%) while allowing a significant reduction in In_2O_3 refractive index. This unique dispersion offers excellent surface coverage and three-dimensional volumetric expansion compared to a thin film, and a step reduction in refractive index compared to bulk active materials or randomly porous composites, to more closely match the refractive index of an electrolyte, improving transparency. The (111) surface orientation of the nanodots, when fully ripened, allows minimum lattice mismatch strain between the In_2O_3 and the Si surface. This helps to circumvent potential interfacial weakening caused by volume contraction due to electrochemical reduction to lithium, or expansion during lithiation. Cycling under potentiodynamic conditions shows that the transparent anode of nanodots reversibly alloys lithium with good Coulombic efficiency, buffered by co-insertion into the silicon substrate. These properties could potentially lead to further development of similarly controlled dispersions of a range of other active materials to give transparent battery electrodes or materials capable of non-destructive *in-situ* spectroscopic characterization during charging and discharging.

Introduction

The marked increase in portable electronic device sales together with huge demand for flat screen high-definition televisions (HDTVs) are the main driving forces behind the need for batteries and continued research into various materials and forms for transparent conducting oxides (TCOs) and similar coatings. Among TCOs, materials such as indium oxide (IO), tin oxide (TO) or tin-doped indium oxide (ITO) [1–6] and emerging alternatives such as graphene and Cu or Ag NWs for example [7,8], have been a consistent focus of research interest [9] where transparency is a useful visible range or indeed other wavelength regions of interest, is matched by sheet resistances below 10 Ω/□ [10]. ITO is the TCO used most often and its applications vary from thin film transistors [2,6,11–13], optical circuits [14], displays [15,16], touch screens [17], and also as a transparent contact in solar cells [5,18–20]. Low sheet resistances are typically required for thin-film solar cells and the solar photon flux-weighted optical transparency of ITO on glass is about 80%. The battery however, a key component in the majority of portable electronics, has only very recently been demonstrated as a transparent device [21], and scope exists for the development of true see-through charge storage materials [22–28], where touch screens, solar cells and charge storage batteries can co-exist with transparent, or optically addressable form.

Their metallic properties cause most TCO's to be reflective in the infrared and for most TCO's a trade-off exists between transparency and conductivity, and sheet resistance for thin films [29]. In line with this, transparency in battery electrodes gives the opportunity for *in-situ* and non-destructive diagnostic analysis of material changes during operation and the development of conductive current collectors and electrode materials that reversibly intercalate lithium with sufficiently high volumetric energy densities. This research could also allow the possibility of investigating kinetics of insertion mechanisms and the influence

of certain lithiated phases of TCO materials on transparency and conductivity. This is critical for the analysis and development of both new battery materials and chemistries, but also for the examination of TCO materials for charge storage applications [30–34].

Transparency can be provided by using miniscule quantities of materials, or very thin films of uniform deposits[35], but to have functioning volumetric energy densities, strategies to improve transparency while maximizing active material coverage of an electrode would be advantageous. The only formally transparent element in a typical battery is its electrolyte, which is soaked into a porous polymeric membrane and sealed with opaque materials between two sheets of metal. One method to allow transparency in a battery is to reduce active material dimensions below their optical absorption length; there are no currently used battery materials with absorption lengths that are sufficiently long in the full potential window in which the battery operates. Architectures of materials that influence optical properties have shown promise in this regard, but it does not automatically apply to small or quantities of active materials or porous materials; a graded or step-change in refractive index from high to low is typically required to minimize Fresnel reflections, enhance transparency and its angular dependence to longer wavelengths. Varying surface coverage using dispersions that promote UV, visible and NIR transparency is also possible and the transparency window can be tuned by controlled variation of materials dispersion, the variation in refractive index throughout the material and its inherent electronic and optical properties [2-6]. The recent demonstration of a fully transparent battery prototype [20] also involved testing of a continuous In_2O_3 thin film electrode. During cycling however, it was found that metal nanodots and lithium oxides and peroxides formed to such an extent that transparency was significantly reduced.

Here, In_2O_3 {111}-oriented crystalline nanodot dispersions have been successfully grown from an MBE deposition of an In layer and subsequent oxidation at elevated

temperature. The method results in unique areal and size dispersions of nanodots varying in size from hemispherical 2 nm dots to larger, faceted ~500 nm crystals, on the Si current collectors. Angle-resolved transmittance measurements confirm that the deposits maximize transparency in the infra-red, while maintaining characteristic transparency in the visible with a beneficial reduction in resistivity and sheet resistance; this overcomes the transparency limitations for In_2O_3 nanomaterials by index matching through a unique size dispersion and reduction in refractive index from the current collector to the electrolyte. The nanodots form as $In@In_2O_3$ core-shell crystals, and form a stable solid electrolyte interphase (SEI) layer and reversibly alloy with lithium allowing them to function as visible-to-IR transparent, visibly antireflective Li-ion battery electrodes. These properties could potentially lead to further development of similarly controlled dispersions or graded index (porosity) of a range of other active materials that facilitates enhanced transparency. The approach shown here is straightforward and scalable and may be applied to the fabrication of high quality optoelectronic, electronic and sensor devices and as a promising route towards visible-to-IR transparent conducting TCOs that reversibly store (electro)chemical charge, and also for the development of non-destructively, optically addressable materials and interfaces for *in-situ* monitoring of electrochemical processes.

Experimental section

Before growth on silicon and glass substrates, the respective surfaces were cleaned using a standard RCA process. After rinsing, a second treatment in a H_2O_2:HCl:H_2O (1:1:5) solution was used to remove metallic and organic contamination. For evaporation of the In sources, a home-built MBE high-vacuum chamber with a distinct effusion cell for In together with an electron-beam evaporator, was designed in cooperation with MBE-Komponenten GmbH, with calibrated growth rates. As detailed Fig. 1, a uniform layer of In metal was deposited at

a rate of 0.1 Å s^{-1} at a substrate temperature of 400°C, with precise control over the nominal thickness, (see Supporting Information Section S1 for the details of the deposition process). The associated activation energy for exponential film growth is E_a = -1.435 eV, which is consistent with the literature and calibration values for removal of Indium atoms from the source.

Surface morphologies and the chemical composition of the nanostructured dispersions were investigated by electron microscopy using a Hitachi SU-70 SEM with an Oxford-50mm^2 X-Max detector for energy dispersive X-ray analysis and Oxford Instruments Nordlys EBSD detector with HKL Channel 5 acquisition software. TEM analysis was conducted with a JEOL JEM-2100F field emission microscope operating at 200 kV, equipped with a Gatan Ultrascan CCD camera and EDAX Genesis EDS detector for atomic resolution crystal structure and composition examination. The size distribution of the nanodots was analysed using ImageJ [36].

X-ray photoelectron spectroscopy was acquired using a Kratos Axis 165 monochromatized X-ray photoelectron spectrometer equipped with a dual anode (Mg/Al) source. Survey spectra were captured at as pass energy of 100 eV, step size of 1 eV, and dwell time of 50 ms. The core level spectra were an average of 10 scans captured at a PE of 25 eV, step size of 0.05 eV, and dwell time of 100 ms. The spectra were corrected for charge shift to the C 1s line at a binding energy of 284.9 eV. A Shirley background correction was employed, and the peaks were fitted to Voigt profiles.

Variable angle spectroscopic ellipsometry (VASE) was performed using a J. A. Woollam Co., Inc. M-2000U variable angle spectroscopic ellipsometer over a wavelength range of 300 to 900 nm. Reflectance measurements were carried out in a Bruker FT-IR spectrometer IFS66/V on nanodot samples and ITO on glass. Different configurations of beam splitters, detectors and sources were used to cover the infrared (5 μm) to visible ranges.

For angular resolved measurements, a NIR512 Ocean Optics spectrometer was used as a detector in a home-built reflectance/transmittance setup using a collimated Xenon arc lamp as a light source.

To investigate the electrochemical insertion (alloying) and removal of Li, cyclic voltammetry measurements were carried out in a 3-electrode setup using a Multi Autolab 101 potentiostat, using Li as both counter and reference electrodes. All potentials, unless otherwise stated, are relative to Li^+/Li. Custom build swagelock-type cells were used with counter and active material electrode separated by a polypropylene separator soaked in 1 mol dm^{-3} solution of $LiPF_6$ in EC:DMC at a 50:50 v/v ratio. The electrode was cycled at a scan rate of 0.5 mV/s. Afterwards, the electrode was carefully washed in acetonitrile and a 10^{-4} mol dm^{-3} solution of acetic acid to remove the electrolyte residue.

Results and discussion

Figure 1a shows a SEM image of the nanostructures grown by MBE of indium in an oxygen atmosphere. The MBE deposition was conducted at a rate of 0.1 Å s^{-1}; such a slow deposition rate is typically used to ensure initial seeding of the substrate with a metallic seed layer [37]. Subsequent oxidation in ambient air allows the formation of a specific size dispersion of oxide crystals after In growth, as shown in Fig. 1b. The dispersion consists of larger crystals interspersed with a high density of very small (~2-5 nm) nanodots (Fig. 1c). Some of the larger crystals have clearly developed facets (Fig. 1d), generally growing in a deviated hexagonal shape (Fig. 1e). High resolution SEM images of the nanodots show that a number of small crystallites are found on the top surfaces of the crystals in a hierarchical fashion (Fig. 1d).

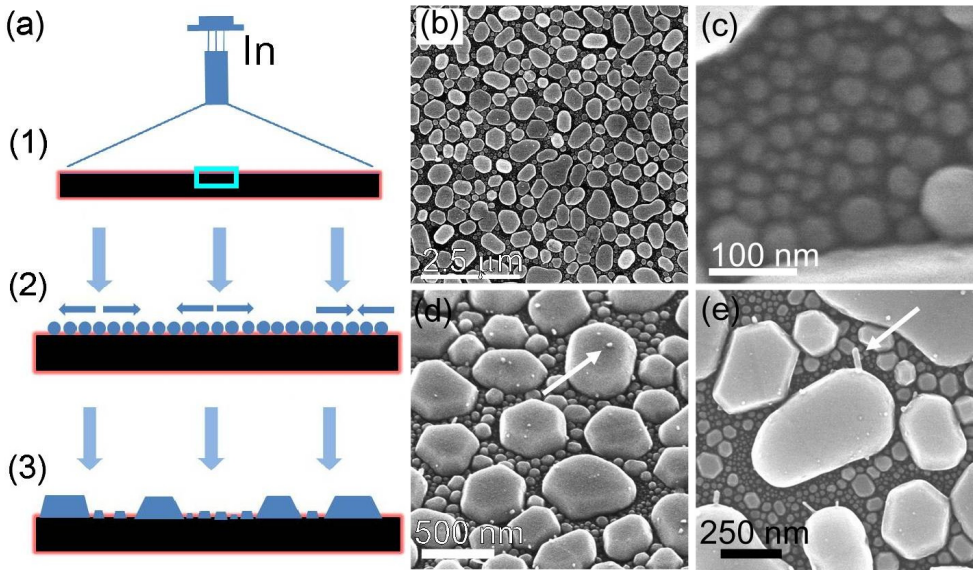

Figure 1. (a) Schematic of the MBE growth steps for In_2O_3 nandot dispersions from In deposition, wetting layer formation and oxidative crystallization. (b) SEM image showing the final epitaxial In_2O_3 nanodot dispersion on Si. (c) SEM image showing small, hemispherical nanodots interspersed between larger crystals. The arrow indicates small crystallites growing hierarchically on the top surfaces of larger crystals. (e) SEM image of frustrated-faceted nanodots (which are also single crystal). The arrow indicates nanowire growth from the edges of the crystals.

The initial formation of a dewetted liquid In 'layer' comprising a high density of metallic nanodots (maintained in a liquid state on a substrate heated to 400 °C), and the progressive nature of their deposition allows hierarchical nanodot seeds to form on the high energy facet edges of the larger crystals. In some cases we observe subsequent growth of long, straight In_2O_3 nanowires (see Fig. 1e) with lengths reaching hundreds of nanometres and diameters not exceeding the diameter of hierarchical dots. The nanodot dispersions (and also the progressively nucleated dots-on-dots) form by thermally driven (substrate heating) ripening, coalescence, oxidation crystallization, and continued progressive In deposition.

It was previously shown by Hao *et al.* that the surface energy of the main faces during growth of In_2O_3 crystals (and many crystals in general) follow a gradient in surface free energy and subsequent growth rates, *i.e.* $\gamma[111] < \gamma[100] < \gamma[110]$ [38]. In low saturation MBE deposition, these relationships greatly influence the final shape of the nanodots. We used electron backscattered diffraction from the terminating surfaces of both faceted and non-faceted nanodots to quantify their epitaxial relationship to their substrate and also their relative orientational distribution. The measurements were taken at 70° tilt (Fig. 2a) and a pole plot of the nanodot texture orientation distribution (Fig. 2b) was formed by monitoring the Kikuchi diffraction patterns from the top surface lattice planes of the nanodots shown in Figs 2c and d; the growth orientations from 3D crystal symmetry are visible as diffraction 'paths' in orientation-space. The measurements confirm a dominant {111} surface termination for the nanodots. Interestingly, for both faceted and non-faceted crystals, their terminating planes are near-identical, as are their overall heights of ~50 nm, see Fig. 1d. Any 'flow' of material pre-oxidation occurs almost entirely parallel to the substrate and thus a perfect faceted crystal is not required to give an iso-terminated nanodot dispersion.

Being extremely sensitive to tilt or variations in the top surface of the crystals, the corresponding pole plot shown in Fig. 2b were acquired to map the distribution of textures around major growth directions. The texture pole plot is centered around the {111} directions. It is clear from the texture distributions in the in Fig. 2b, that the particles grow with horizontal hexagonal {111} planes, parallel to the (100) substrate of the silicon wafer. The three areas of high frequency distribution located around 70.5 degrees is related to similarity between {111} plane equivalent planes: (111), (-111), (1-11) as well as (11-1) growth directions. The In_2O_3 nanodots were epitaxially deposited as metal nanodot seeds and subsequently oxidized in air and EBSD analysis confirms that their oxidation to In_2O_3 nanodots results in a final single crystal structure with the slowest {111} growth planes

parallel to the substrate. Pole plots of the dispersion of the texture of the nanodots around remaining two pole directions are shown in Supporting information Fig. S2, indicating angular relationships between growth planes and polar directions.

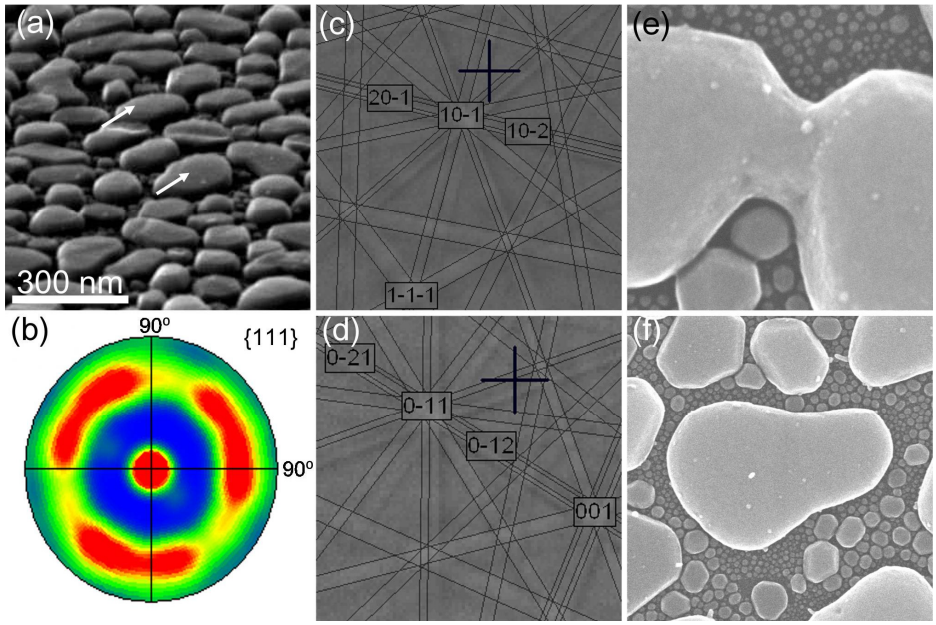

Figure 2. (a) SEM image of the In_2O_3 nanodots. Arrows indicate the location of the points at which the EBSD pattern was recorded. (b) Pole figure showing the relative orientation distribution of {111} termination of the nanodots. (c-d) Kikuchi band overlays recorded from the regions indicated in (a). The cross on each image indicates the orientation of the planes at their measurement point. (e) Two In_2O_3 crystals imaged during coalescence. (f) Fully coalesced crystal with no discernible boundary between individual merged nanodots.

A three-fold symmetry with three distinct peaks of similar intensity was observed in pole figure of {111} reflections and consists of the central [111] zone axis (centre pole) and [-111], [1-11] and [11-1] at 70.5°from the centre pole. Different rotations of the growth plane can be seen in the equivalent cell representations in Supporting Information Fig. S3, acquired

from individual diffraction measurements from the surface of a number of separate nanodots. The growth rate perpendicular to {111} planes is comparatively slower than {110} and {100} planes. As a result, growth in lateral direction progresses faster than in vertical, which we find regardless of the degree of crystal faceting. Such arrangement results in formation of truncated octahedral structures, that coalesce with their nearest neighbours during growth (see Fig. 2e). In such cases, the reason for the formation of non-faceted particles can results from reflow of metallic In with next nearest neighbours (necking and ripening), which was captured after solidifying oxidative crystallisation in Fig. 2f.

One of the important factors in MBE growth of oxide films and particularly when these materials undergo volume expansion during uptake of Li ions during charging, is the quality of physical contact to the substrate, indicated by the lattice mismatch $f = (a_f - 2a_{sub})/2a_{sub}$, where a_f and a_{sub} are the lattice constants in the growth plane of In_2O_3(111) and Si(100), respectively. The mismatch parameter should be as low as possible to minimize the additional strain placed on the deposit due to electrochemical reduction from In_2O_3 to metallic In and subsequently during volumetric expansion accompanying electrochemical Li-alloying. For In_2O_3, the (111) lattice parameter is 1.074 nm, leaving a mismatch of 1.13% between a_f and $2a_{sub}$ (for a Si(100) lattice spacing of 1.086 nm). The resulting strain between the nanodot-substrate interface is low; the surface free energy of In_2O_3(111) is much lower than that of Si(100) [39]. This orientation offers the least possible interfacial strain between In_2O_3 and Si(100). The deposition of the first few atomic layers of In results in complete wetting of an area of the surface according to the Frank van-der Merwe (FM) growth mechanism. Subsequent deposition of adatoms causes accumulation of strains and leads to change of growth mechanism from FM to Stranski-Krastanow (SK) resulting in 3-dimensional islands on 2D wetting layer, since the liquid In dewets to form droplets on the surface as the adatom concentration shifts the metastable deposition to an unstable condition

[40]. This qualitatively also explains why we consistently observe nanodots beginning to form *via* a hierarchical mode with smaller length scales on top of crystallizing dots. Although the lattice constant is formally the same for In_2O_3 on In_2O_3, this only holds when the orientation of the crystal deposit matches that of the underlying dot; which this is not the case, strain-relieved dots-on-dots are possible.

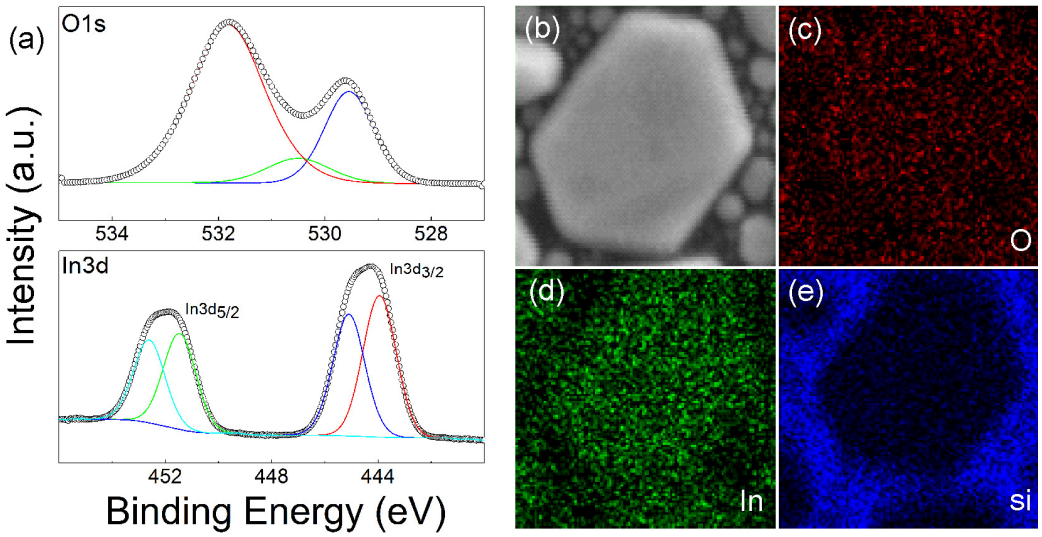

Figure 3. X-ray core-level photoelectron spectra of (a) O 1s and In 3d of the In_2O_3 nanodot dispersion. (b-e) EDX maps of In_2O_3 nanodot showing distributions of oxygen, indium and silicon respectively.

The composition of the MBE nanodots were determined using XPS and EDX. Figure 3a shows the In3d and O1s core-level photoelectron emission spectra of the nanodots. Core-level emission corresponding to In $3d_{5/2}$ and In $3d_{3/2}$ were observed at 444.34 eV and 452.03 eV (referenced to the C1s core-level of 284.9 eV, see Supporting Information, Fig. S4), indicative of In_2O_3. The peak at 444.34 eV shows hyperfine levels, one at 443.9 eV from In(0) and at 445.1 eV related to In $3d_{5/2}$ from In_2O_3. Core-level emission from O 1s was composed of two spectral bands at 531.2 eV and 529.6 eV, which can be deconvoluted into

three components consistent with In_2O_3. The signal at 531.2 eV is attributed to lattice oxygen, while that at 529.6 eV stems from some $In(OH)_3$, which is known to form from exposure of In_2O_3 to water vapour. Corresponding EDX maps of In and O (shown in Figs 3b-e) corroborate oxide composition of the nanodots.

In_2O_3 nanodot dispersions and electrode coverage

To determine the coverage of the nanodot dispersions, we analysed their size distribution by factoring the anisotropy in non-hemispherical shape. Due to the large variance in sizes and asymmetrical shapes, the Feret diameter (the distance between two parallel tangents at arbitrary angle, defined in Fig. 4) is used to describe a shape-nulled size distribution, shown in Figs 4a-d. Complete Feret data provides a rich source of information of particle shape that allow determination of particle shape descriptors and the details of this analysis are outlined in the Supporting Information, Section 2 and from image analysis of nanodot distributions shown in Fig. S5.

Figure 4a shows the distribution of In_2O_3 nanodots interspersed between the larger surface crystals (Fig. 4b). At the end of growth, these particles coarsen during dewetting of the liquid In during progressively deposited and crystallizing nanodots. In this case, the deposition has a dynamically changing free surface area. The overall bimodal distribution, confirmed by the existence of two peaks in the histogram in Fig. 4d, results in a high degree of surface coverage, with the nanodots at ripening-coalescence stage of growth comprising ~60% of the sample surface and ~10% of the sample surface covered with nanodots in the nucleation-ripening stage of growth. The overall mass distribution is estimated to be ~70 µg cm^{-2}. Figure 4d represents the final size distribution from oxidative crystallization. The size distributions at the respective length scale as seen by SEM are shown in Figs 4c and d.

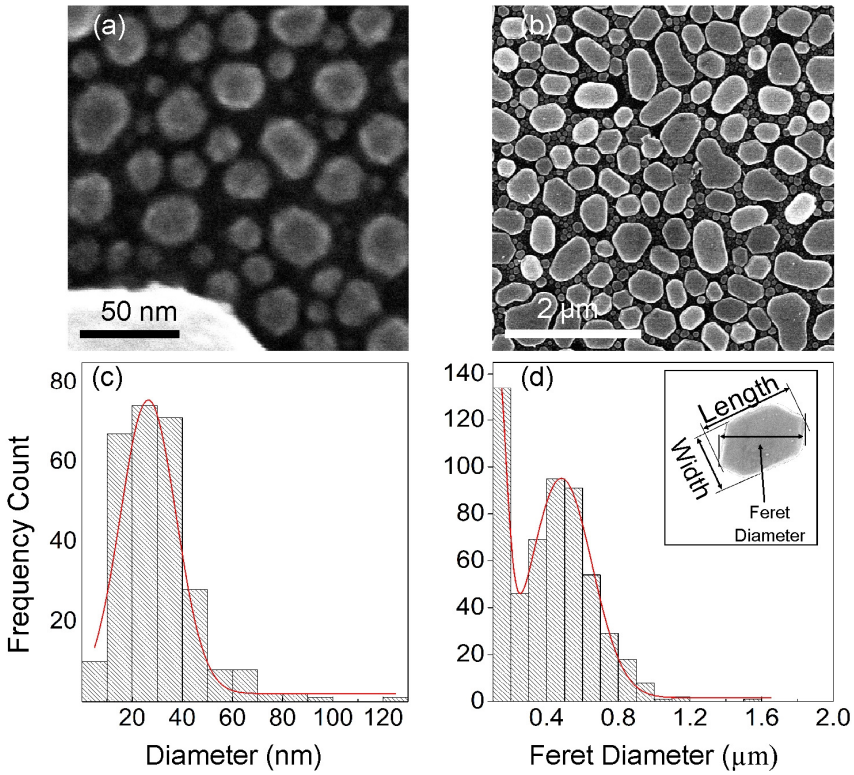

Figure 4. Feret diameter distribution histograms for In_2O_3 nanodots. (a) Nucleation and ripening mode, (b) ripening and coalescence mode. The inset shows indicates how the Feret Diameter of a nanodot is defined for this work. (c) SEM image showing particles with growth distribution described in (a), and (d) SEM image showing nanodots with the growth distribution described in (b).

The existence of two primary peaks in the size distributions suggests a two-stage overall growth mechanism (Supporting Information Section 3) [41]. Firstly, nucleation and ripening of adatom species from MBE results in the formation of small nanocrystals on the surface of the silicon, with a maximum eventual average size determined to be ~30 nm. Continuous ripening growth of the nanodots results in their growth and transition from nucleation and ripening, to ripening, coalescence and further growth (including a second phase of nucleation on the surface of nanodots already on the surface, as shown in Fig. 1d).

The dispersion with two primary length scales allow a particular in-plane porosity of ~20% with maximal associated areal coverage of the substrate.

Enhanced IR transparency of the In_2O_3 nanodot dispersions

In_2O_3, as a wide bandgap semiconductor (E_g^d ~ 3.6 eV; E_g^i ~ 2.6 eV), has a transparency that is fundamentally interlinked with it conductivity; the transition occurs on or around its plasma frequency related to the electron density according to the Drude model by $\omega_p^2 = nq^2/m^*\epsilon_0$, where m^* and q are the effective mass and charge of an electron, and ϵ_0 the high-frequency permittivity of free-space. For the single-sided In_2O_3 nanodot dispersion, the transmission is limited by Fresnel reflection due to the step discontinuity in refractive index at the rear flat surface [35,42,43], depicted for an ITO film on glass and the nanodots on silicon in Fig. 5. The refractive index of as-received Si(100) substrate is 3.42 and that of In_2O_3 is 1.46 at the interface, which reduces to 1.24 at the nanodots-air interface measured by spectroscopic ellipsometry (see Fig. 5).

The nanodots-air interface is reasonably uniform and analysed as a porous Cauchy layer [44,45]. In our case, the NP nanodots dispersion 'layer' acts as a porous thin film (considering the NP dispersion and their size dispersion), whose refractive index and extinction coefficients, shown in Fig. 5, are different with respect to a bulk film (n = 2.4), forming a several-step reducing index on the material-containing side of the electrode. The reduced nanodot effective refractive index reduces Fresnel reflection within the nanodot dispersion compared to a flat ITO film by reducing the step change in index, enhancing transmission and antireflection. This aspect is crucial for consideration of other active materials in transparent battery investigations. While many composites and nanoscale materials can be deposited with controllable porosities, to enhance transparency and reduce

reflection, a graded or step reduction in the index from the current collector to the electrolyte interface is required.

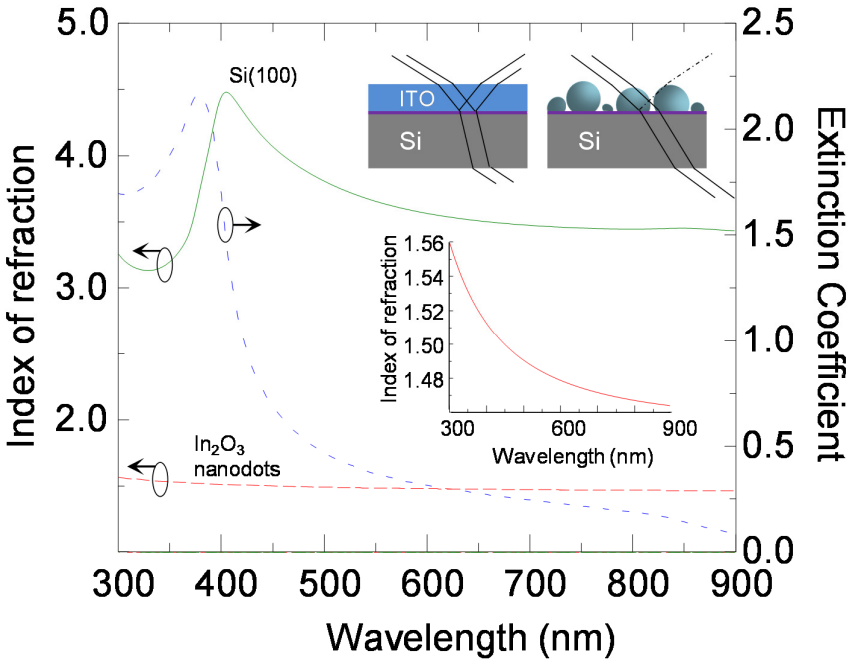

Figure 5. Cauchy dispersion of refractive index and extinction coefficient of the In_2O_3 nanodot dispersion, shown schematically in the inset, on Si(100), measured by spectroscopic ellipsometry. The inset shows the variation of refractive index for the nanodot dispersion as a function of wavelength.

Angle resolved transmission measurements of the nanodot dispersions and an ITO thin film were determined and summarised in Fig. 6. The position of the plasma frequency indicated by ω_p, red shifts and the reflectance of the In_2O_3 nandots dispersion and the ITO thin film decreases with angle near their respective plasma frequencies, shown in Fig. 6a, while the reflectance decreases substantially after the plasma frequency relative to that before the onset of the plasma frequency. These layers offer excellent visible-infrared transmission, and also antireflection properties, as seen in the optical images in Fig. 6b and c. The red-

shifting of the entire angle-resolved spectrum for the nanodots dispersions is also seen in Fig. 6a, where at visible wavelengths the transmission varies from 55% at near incidence and at 40°, and importantly, remains 87% transparent at wavelengths up to 4 μm (Fig. 6a).

Corresponding angle-resolved reflectance of an ITO film in Fig. 6d, confirms a blue-shift of the plasma frequency with increasing angle, but even at normal incidence the comparison comparative ITO film is similarly conductive but much less transparent at IR wavelengths. The nanodot dispersions allow shifting the maximum in transmission (and minimum in normal reflectance) to longer wavelengths while maintaining identical transmission in the same energy window as commercial ITO on glass (Fig. 6a), and with the added benefit of a lower effective sheet resistance into the IR.

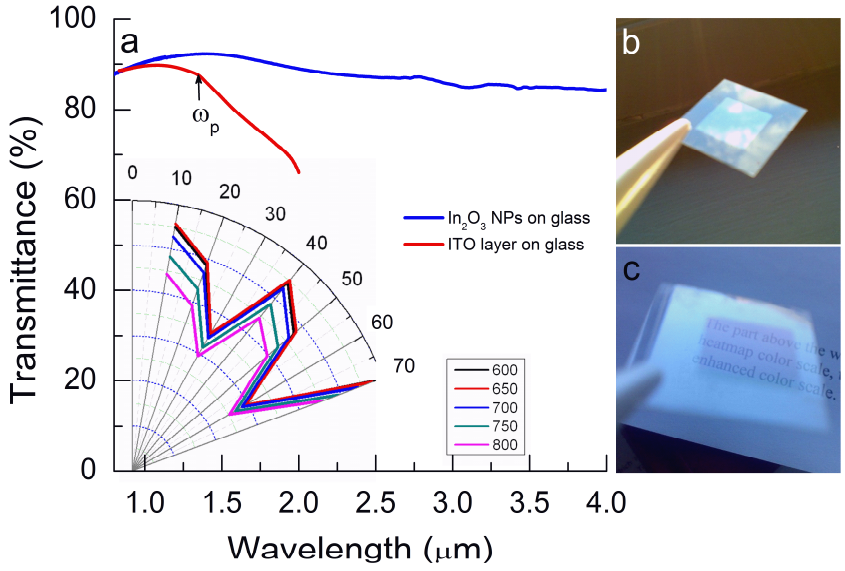

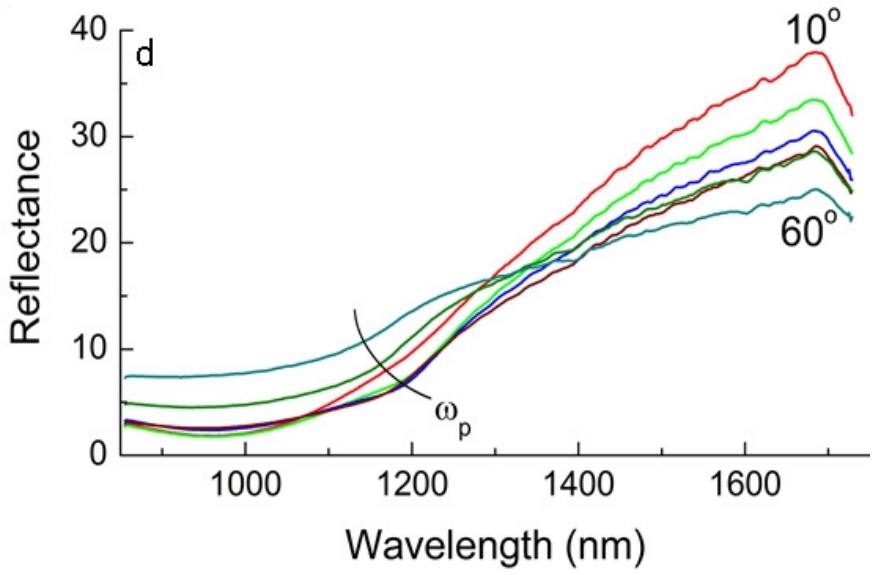

Figure 6. (a) Transmittance of the In_2O_3 nanodot dispersions and that of an ITO thin film of similar nominal thickness. (*Inset*) Polar plot of the angle-resolved transmission of the nanodots at visible wavelengths. (b, c) Optical images of the In_2O_3 nanodots showing antireflection characteristics in the visible range. (d) Angle-resolved reflectance of an ITO film.

Reversible electrochemical Li-insertion

The ability of the In_2O_3 nanodot dispersions to reversibly intercalate or alloy Li, and its insertion and removal potentials, was examined using cyclic voltammetry. Figure 7a shows the cyclic voltammetric response of the Li|Li^+-electrolyte|In_2O_3(111)|Si(100) system. For this cell the cathodic process involved the insertion of Li into In_2O_3 to form a Li-In alloy (charging) and the anodic process follows Li extraction or dealloying (discharging). A related process is known to occur for Li alloying with Sn [46], but there are limited investigations of Li insertion in to In-containing materials [47]. During the first negative scan, two weak irreversible peaks appear at 1.2 V and 0.8 V from the reduction of In_2O_3 to In^0 (see

Supporting Information, Section S4 for electrochemical reduction and alloy processes). Once reduced from In_2O_3 to In^0, the indium is never oxidized again in the potential range examined. Zhou *et al.* [33] have shown reoxidation, but cycled the anode to over 3.5 V, a voltage window typical of cathode materials. We cycled the anode in 0 - 2.5V, a potential window below oxidation potential of In^0 (2.7 V vs. Li^+/Li)[48].

A large reversible peak appears at 0.4 V from the alloying process of Li insertion into In^0. The rate of this reaction, indicated by measured current is found to reduce with increasing cycle number. The reversible Li insertion-removal process occurs in a voltage window of 0.4 – 0.7 V are the reversible processes described by $zLi^+ + ze^- + In \leftrightarrow Li_zIn \quad (0 < z \leq 4.33)$. For the Li|$Li^+$-electrolyte|$In_2O_3$(111)|Si(100), buffering of polarization effects is provided by the Si current collector, which can accommodate the highest Li storage capacity of all anode materials [49,50].

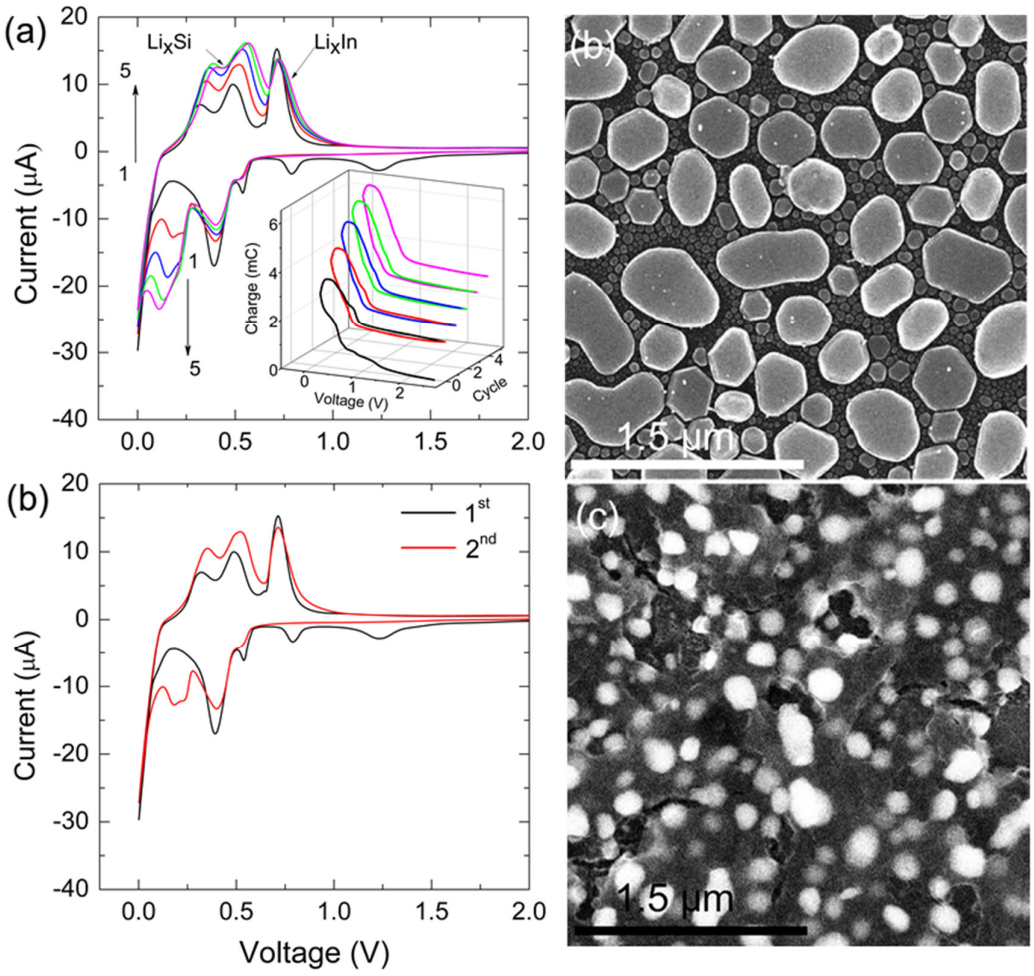

Figure 7. (a) Cyclic voltammetry of In_2O_3 nanodot electrodes between 0.0 - 2.5 V. Inset shows the corresponding integrated charge vs. voltage curve for 5 cycles. (b) Cyclic voltammograms for first and second cycle highlighting the SEI layer formation. Arrows indicate phases formed during insertion and removal processes. SEM images show the nanodots before (c) and after cycling (d).

The free surface area (~20%) between neighbouring particles allows Li to be co-inserted into the silicon current collector, which is indicated by the existence of two additional peaks in the anodic part of the insertion reaction, at 0.32 V and 0.5 V. Those peaks relate to the removal of lithium from silicon [49]. Figure 7b shows the first 2 cycles of this

system, and we note that the reduction of In_2O_3 and related alloying processes dominate over Li_xSi phase formation and insertion of lithium into silicon in the first cycle. This co-insertion into the active material and current collector equilibrates after the second cycle. The increasing rate of Li-Si formation can be attributed to an activation effect [51] linked to lithiation-induced volumetric expansion that causes cracking and the exposure of unreacted material to the electrolyte. Successive cycling then allows more lithium to intercalate into silicon, providing a degree of stress buffering for the In alloying process without requiring carbon, conductive additives or polymeric binders. The rate of alloying and dealloying, insertion and removal are consistently balanced in each cycle (Fig. 7, inset), and apart from charge associated with SEI formation and reduction to In^0, negligible charge fading is found for *all* processes in all subsequent cycles.

During co-insertion into the active material and current collector, both of which are reversible, the variation in volumetric changes and accompanying effects is considered. The SEM images in Figs 7c and d show the condition of the electrode surface before and after cycling. Using the size distribution analysis (*cf.* Fig. 4), the reduction in average nanodot size is 30-50% . The brightness of the secondary electron emission stems from a reduced conductivity of the Li_xIn phase. As the nanodots are epitaxial, their adhesion to the substrate is excellent, and lithium insertion is not likely to occur directly under each nanodot, unless they are extremely small. In this case, we note (Supporting Information, Fig. S6), that some of the smallest nanodots are removed from the substrate, but this occurs when their diameter is less than the change in volume of the near surface of the silicon. The molar volume of In^0 is a factor of 2.45 less than the In_2O_3 and by comparison to the size reduction observed, it is clear that no significant volume change effects occur in stable In^0 nanodots [52]; faceting related to the structure of In_2O_3 is also lost during electrochemical reduction to the pure metal.

Previous reports show that the electrochemical performance of In_2O_3 is strongly influenced by its microstructure and composition [32]. Here, the dispersion of the nanodots, while permitting transparency and conductivity into the IR region, also allows lithium insertion into the current collector, and remains structurally stable due to strong epitaxial adhesion and lithium co-insertion buffering by the silicon current collector. The partial porosity of the variable size nanodot distribution prevents stress build up in the In^0 (when reduced from In_2O_3) and promotes optical transparency. The removal of the smallest nanodots by volume expansion of the underlying silicon does not largely affect the gravimetric energy density, and it serves to buffer polarization of the Li_xIn by reversibly inserting Li^+. Detailed size distribution analysis before and after cycling shows that some volume expansion occurs in the alloyed Li-In phase, but it does not affect the structural integrity of the electrical contact to the current collector.

Conclusions

The unique size dispersion of In_2O_3 nanodots prepared by MBE deposition of indium and subsequent oxidation in air at elevated temperature, has allowed the development of a Li-ion battery electrode with enhanced IR transparency with sacrificing electrical conductivity, and lithium co-insertion processes with high Coulombic efficiency that results in stable cycling and charge storage. The In_2O_3 nanodots show bimodal size distribution confirming a two step epitaxial growth mechanism, and good surface coverage with unique shape and (111) crystalline orientation. The nanodot dispersions were successfully shown to reversibly alloy with lithium after reduction to metallic indium; the specific size distributions allow reversible lithium co-insertion with a silicon current collector as well as the active material on the surface. Moreover, the specific size offers excellent antireflective properties and enhanced

transparency reaching ~87% at 4 μm. By controlling a reduction in refractive index form the current collector to the air or electrolyte interface, active charge storage materials can show improved transparency over wider wavelength ranges. This potentially allows for further development of transparent battery electrodes or the possibility for in-situ non-destructive spectroscopic monitoring of structural and electrochemical processes.

References

[1] Chiu C H, Yu P, Chang C H, Yang C S, Hsu M H, Kuo H C and Tsai Ma 2009 *Opt Express* **17** 21250–6

[2] Chen P-C, Shen G, Chen H, Ha Y, Wu C, Sukcharoenchoke S, Fu Y, Liu J, Facchetti A, Marks T J, Thompson M E and Zhou C 2009 *ACS Nano* **3** 3383–90

[3] Armstrong N R, Veneman P A, Ratcliff E, Placencia D and Brumbach M 2009 *Acc Chem Res* **42** 1748–57

[4] Kim J K, Chhajed S, Schubert M F, Schubert E F, Fischer a. J, Crawford M H, Cho J, Kim H and Sone C 2008 *Adv Mater* **20** 801–4

[5] O'Dwyer C, Szachowicz M, Visimberga G, Lavayen V, Newcomb S B and Torres C M S 2009 *Nat Nanotechnol* **4** 239–44

[6] Yu H K, Dong W J, Jung G H and Lee J-L 2011 *ACS Nano* **5** 8026–32

[7] Hsu P-C, Wu H, Carney T J, McDowell M T, Yang Y, Garnett E C, Li M, Hu L and Cui Y 2012 *ACS Nano* **6** 5150–6

[8] Kim K S, Zhao Y, Jang H, Lee S Y, Kim J M, Kim K S, Ahn J-H, Kim P, Choi J-Y and Hong B H 2009 *Nature* **457** 706–10

[9] Ohta H and Hosono H 2004 *Mater Today* **3** 42–51

[10] Lee J-Y, Connor S T, Cui Y and Peumans P 2008 *Nano Lett* **8** 689–92

[11] Lin D, Wu H, Zhang R and Pan W 2007 *Nanotechnology* **18** 465301

[12] Kim S, Ju S, Back J H, Xuan Y, Ye P D, Shim M, Janes D B and Mohammadi S 2009 *Adv Mater* **21** 564–8

[13] Samedov K, Aksu Y and Driess M 2012 *Chem Mater* **24** 2078–90

[14] Schmidt H, Flügge H, Winkler T, Bülow T, Riedl T and Kowalsky W 2009 *Applied Phys Lett* **94** 243302

[15] Wang Y, Lu L and Wu F 2010 *Nanoscale Res Lett* **5** 1682–5

[16] Wu H, Hu L, Carney T, Ruan Z, Kong D, Yu Z, Yao Y, Cha J J, Zhu J, Fan S and Cui Y 2011 *J Am Chem Soc* **133** 27–9

[17] Kee Y Y, Tan S S, Yong T K, Nee C H, Yap S S, Tou T Y, Sáfrán G, Horváth Z E, Moscatello J P and Yap Y K 2012 *Nanotechnology* **23** 025706

[18] Rider D a, Tucker R T, Worfolk B J, Krause K M, Lalany A, Brett M J, Buriak J M and Harris K D 2011 *Nanotechnology* **22** 085706

[19] Kim H W, Kim H S, Na H G, Yang J C, Choi R, Jeong J K, Lee C and Kim D Y 2010 *J Solid State Chem* **183** 2490–5

[20] Wan Q, Song Z T, Feng S L and Wang T H 2004 *Appl Phys Lett* **85** 4759

[21] Yang Y, Jeong S, Hu L, Wu H, Lee S W and Cui Y 2011 *Proc Natl Acad Sci U S A* **108** 13013–8

[22] Wu Z, Chen Z, Du X, Logan J M, Sippel J, Nikolou M, Kamaras K, Reynolds J R, Tanner D B, Hebard A F and Rinzler A G 2004 *Science* **305** 1273–6

[23] Barnes T M, Wu X, Zhou J, Duda a., van de Lagemaat J, Coutts T J, Weeks C L, Britz D a. and Glatkowski P 2007 *Appl Phys Lett* **90** 243503

[24] Zhang M, Fang S, Zakhidov A a, Lee S B, Aliev A E, Williams C D, Atkinson K R and Baughman R H 2005 *Science* **309** 1215–9

[25] Kim H-K, Kim D-G, Lee K-S, Huh M-S, Jeong S H, Kim K I and Seong T-Y 2005 *Appl Phys Lett* **86** 183503

[26] Gu G, Bulović V, Burrows P E, Forrest S R and Thompson M E 1996 *App Phys Lett* **68** 2606

[27] Chen Z, Cotterell B, Wang W, Guenther E and Chua S 2001 *Thin Solid Films* 202–6

[28] Forrest S R 2004 *Nature* **428** 911–8

[29] King P D C and Veal T D 2011 *J Phys Condens Matter* **23** 334214

[30] Poizot P, Laruelle S, Grugeon S, Dupont L and Tarascon J M 2000 *Nature* **407** 496–9
[31] Kim D-W, Hwang I-S, Kwon S J, Kang H-Y, Park K-S, Choi Y-J, Choi K-J and Park J-G 2007 *Nano Lett* **7** 3041–5
[32] Ho W-H, Li C-F, Liu H-C and Yen S-K 2008 *J Power Sources* **175** 897–902
[33] Zhou Y, Zhang H, Xue M, Wu C, Wu X and Fu Z 2006 *J Power Sources* **162** 1373–8
[34] Wan N, Xu J, Chen G, Gan X, Guo S, Xu L and Chen K 2010 *Acta Mater* **58** 3068–72
[35] Poitras D and Dobrowolski J a 2004 *Appl Opt* **43** 1286–95
[36] Schneider C a, Rasband W S and Eliceiri K W 2012 *Nature Methods* **9** 671–5
[37] Kratzer P and Scheffler M 2002 *Phys Rev Lett* 0361021-4
[38] Hao Y, Meng G, Ye C and Zhang L 2005 *Cryst Growth Des* **5** 1617–21
[39] Follstaedt D M 1993 *Appl PhysLett* **62** 1116
[40] Chambers S A 2000 *Surf Sci Rep* **39** 105–80
[41] Jeong J I and Choi M 2005 *J Colloid Interface Sci* **281** 351–9
[42] Xi J Q, Kim J K and Schubert E F 2005 *Nano Lett* **5** 1385–7
[43] Loncar M 2008 *Nature Photonics* **2** 76–76
[44] Dobrowolski J A, Poitras D, Ma P, Vakil H and Acree M 2002 *Appl Opt* **41** 3075–83
[45] Yoldas B E and Partlow D P 1984 *Appl Opt* **23** 1418
[46] Chen J S and Lou X W (David) 2012 *Mater Today* **15** 246–54
[47] Geaney H, Kennedy T, Dickinson C, Mullane E, Singh A, Laffir F and Ryan K M 2012 *Chem Mater* **24** 2204–10
[48] Vanhees J, Francois J P and Van Poucke L C 1981 *J Phy Chem* **85** 1713–8
[49] Chan C K, Peng H, Liu G, McIlwrath K, Zhang X F, Huggins R a and Cui Y 2008 *Nat Nanotechnol* **3** 31–5
[50] Chan C K, Patel R N, O'Connell M J, Korgel B A and Cui Y 2010 *ACS Nano* **4** 1443–50
[51] Lee B-S, Son S-B, Park K-M, Seo J-H, Lee S-H, Choi I-S, Oh K-H and Yu W-R 2012 *J Power Sources* **206** 267–73
[52] It has been found that translational, compressive and other forces during cell assembly and disassembly cause some of the active material to detach.

Acknowledgements

MO acknowledges the support of the Irish Research Council under award no. RS/2010/2170. WK and CMST acknowledge support from the Spanish MINECO projects ACPHIN (FIS2009-10150) and TAPHOR (MAT2012-31392), the CONSOLIDER project nanoTHERM (CSD2010-00044) and the Catalan AGAUR grant 2009-SGR-150. COD acknowledges support from Science Foundation Ireland under award no. 07/SK/B1232a. The authors thank F. Laffir and C. Dickinson for assistance in XPS and EBSD measurements.